

Geophysical Research Letters

RESEARCH LETTER

10.1029/2019GL085877

Key Points:

- A new methodology for the combined inversion of land and marine ERT data is proposed
- Land ERT data are first inverted alone and corrected to account for the water layer present in marine ERT
- A combined inversion with marine and corrected land ERT, constrained by the resistivity distribution calculated from land ERT, is performed

Correspondence to:

T. Hermans,
thomas.hermans@ugent.be

Citation:

Hermans, T., & Paepen, M. (2020). Combined inversion of land and marine electrical resistivity tomography for submarine groundwater discharge and saltwater intrusion characterization. *Geophysical Research Letters*, 47, e2019GL085877. <https://doi.org/10.1029/2019GL085877>

Received 17 OCT 2019

Accepted 14 JAN 2020

Accepted article online 21 JAN 2020

Combined Inversion of Land and Marine Electrical Resistivity Tomography for Submarine Groundwater Discharge and Saltwater Intrusion Characterization

T. Hermans¹  and M. Paepen¹ 

¹Department of Geology, Ghent University, Ghent, Belgium

Abstract Electrical resistivity tomography (ERT) is particularly suited for the characterization of saltwater intrusion and submarine freshwater discharge, given its sensitivity to the electrical conductivity of pore water. A comprehensive survey might combine land ERT collected during low tide and marine ERT acquired with lower sensitivity due to the presence of a seawater layer, most often, inverted separately. In this contribution, we propose a new methodology to jointly invert land and marine ERT acquired along a same profile, bringing them to a common situation at high tide. We first estimate the electrical resistivity distribution under the land profile. Then, we compute a corrected data set for land ERT, simulating a data set collected with the same level of water as the marine ERT. Finally, both land and marine ERT data sets are inverted jointly. We show that the approach allows to better image the freshwater/saltwater distribution across the shoreline.

Plain Language Summary Freshwater aquifers are essential to provide drinking water to the growing World's population. In coastal areas, groundwater resources are thus under pressure, and many coastal aquifers are endangered by the vicinity of seawater. Studying this phenomenon is important but difficult because it takes place at the interface between land and sea. Most often, scientific investigation techniques applied on land and at sea require different processing. This makes their joint interpretation difficult. One of the available techniques to study freshwater and saltwater in aquifers is electrical resistivity tomography (ERT). Marine ERT is less sensitive because it is acquired at sea, but it can still bring relevant information. In this contribution, we develop a new methodology to allow the joint interpretation of land and marine ERT. This allows us to provide a common image of the freshwater/saltwater interface, which can be further used by scientists or authorities to better manage coastal aquifers.

1. Introduction

Electrical resistivity tomography (ERT) is one of the most versatile geophysical methods (Loke et al., 2013). Its sensitivity to water electrical conductivity makes it well suited for the characterization of the distribution of saltwater intrusion (SI) in coastal aquifers (Attwa et al., 2011; Goebel et al., 2017; Hermans et al., 2012; Nguyen et al., 2009). Submarine groundwater discharge (SGD) is an integral part of the dynamical equilibrium of coastal aquifers. It constitutes the outlet to the sea of freshwater infiltrating on land mixed with recirculated saltwater (Kwon et al., 2014; Taniguchi et al., 2002; Zhou et al., 2019). SGD from shallow aquifers occurs from the intertidal zone to hundreds meters offshore depending on the (hydro)geological conditions (Bratton, 2010; Post et al., 2013).

Although ERT remains suited for the characterization of SGD, its location at the limit between terrestrial and marine realms makes it more challenging, as it requires data acquisition both on land and at sea. Land-based ERT with electrodes lying on the seafloor is possible (Henderson et al., 2010; Taniguchi et al., 2006), but the extension is physically limited by the length of the cable. Marine ERT with electrodes at the surface of the sea or dragged on the sea bottom constitutes a fast way to collect data (Befus et al., 2014; Cardenas et al., 2010). However, its resolution and depth of investigation are worse than classical land ERT profiles, because most of the electrical current flows into the sea (Henderson et al., 2010).

In practice, when both land and marine ERT are present, they are inverted separately and qualitatively integrated into a common interpretation. Nevertheless, for a comprehensive understanding of saltwater intrusion and SGD, profiles across the shoreline are needed, combining both methods, ideally with

some overlapping to limit gaps and lower sensitivity zones within the section. This can be done by acquiring land ERT data at low tide and marine ERT at high tide. Although tides induce very dynamic conditions, the water level remains stable around low and high tides, allowing to acquire data without influence of the changing tide. This approach introduces a bias between the data sets due to the presence of the seawater column. As shown by Henderson et al. (2010), the presence of the seawater leads to strong distortions, depending on the thickness and electrical conductivity, if it is not accounted for in the inversion. In this contribution, we propose a new methodology to jointly invert land and marine ERT acquired along the same profile.

2. Method

2.1. Data Correction

Consider a cross-section across the shoreline at low tide, land ERT data are acquired, either with the last electrode located at the low water line or with underwater electrodes. The corresponding data set is $\mathbf{d}_{land, lw}$, where lw refers to low water level, with a corresponding noise level $\epsilon_{land, lw}$. At high tide, marine ERT data are acquired with floating electrodes or electrodes dragged on the sea bottom. The corresponding data set is $\mathbf{d}_{sea, hw}$, where hw refers to high water level, with a corresponding noise level $\epsilon_{sea, hw}$. Note that the methodology does not require low water and high water conditions to correspond to high and low tide.

To jointly invert both data sets, a common situation should be considered. Since marine ERT cannot be simulated at low water level (absence of water), the common situation is considered at high water level. However, the presence of the seawater layer prevents the direct use of $\mathbf{d}_{land, lw}$ for inversion. To overcome this limitation, we propose to compute a corrected data set for land ERT at high water level $\mathbf{d}_{land, hw}$. Estimating the latter data set requires the true distribution of electrical resistivity, which constitutes the unknown of the problem.

We adapt the methodology developed by Hayley et al. (2010) to correct time-lapse ERT data sets for variation in temperature to calculate $\mathbf{d}_{land, hw}$. The data measured on land at low water level are related to the distribution of electrical resistivity in the subsurface

$$\mathbf{d}_{land, lw} = \mathbf{G}(\mathbf{m}_{true}) + \epsilon_{land, lw}, \quad (1)$$

where \mathbf{G} is the forward mapping operator and \mathbf{m}_{true} is the unknown distribution of electrical resistivity. Assume that we could measure the same data set at high water level. We would have

$$\mathbf{d}_{land, hw} = \mathbf{G}(\mathbf{m}_{true} + \Delta\mathbf{m}) + \epsilon_{land, hw}, \quad (2)$$

where $\Delta\mathbf{m}$ represents the modification in electrical conductivity due to the presence of seawater above the electrodes and $\epsilon_{land, hw}$ the corresponding noise level. Using Taylor's first-order approximation, we have

$$\mathbf{G}(\mathbf{m}_{true} + \Delta\mathbf{m}) = \mathbf{G}(\mathbf{m}_{true}) + \frac{\partial \mathbf{G}(\mathbf{m}_{true})}{\partial \mathbf{m}} \Delta\mathbf{m} \quad (3)$$

or expressed in terms of data, and assuming that the noise on both data set is similar

$$\mathbf{d}_{land, hw} = \mathbf{d}_{land, lw} + \frac{\partial \mathbf{d}_{land, lw}}{\partial \mathbf{m}} \Delta\mathbf{m}, \quad (4)$$

\mathbf{m}_{true} is unknown. If we make a first estimation \mathbf{m}_{est} by inversion of $\mathbf{d}_{land, lw}$, we obtain the corresponding data set

$$\mathbf{d}_{land, lw}^{est} = \mathbf{d}_{land, lw} + \mathbf{e}, \quad (5)$$

with \mathbf{e} the inversion error. With this model, we can simulate the corresponding data set at high water level

$$\mathbf{d}_{land,hw}^{est} = \mathbf{G}(\mathbf{m}_{est} + \Delta\mathbf{m}). \quad (6)$$

Those two data sets can be used to estimate the derivative in equation (4)

$$\frac{\partial \mathbf{d}_{land,hw}}{\partial \mathbf{m}} = \frac{\mathbf{d}_{land,hw}^{est} - \mathbf{d}_{land,hw}^{est}}{\Delta\mathbf{m}}. \quad (7)$$

Therefore, the land ERT data set corrected at high water level is deduced:

$$\mathbf{d}_{land,hw} = \mathbf{d}_{land,hw} + \frac{\mathbf{d}_{land,hw}^{est} - \mathbf{d}_{land,hw}^{est}}{\Delta\mathbf{m}} \Delta\mathbf{m} = \mathbf{d}_{land,hw} + (\mathbf{d}_{land,hw}^{est} - \mathbf{d}_{land,hw}^{est}). \quad (8)$$

In short, to calculate the correction, one needs to run an inversion to estimate the electrical resistivity model from the land ERT data. From there, one can compute the correction factor to apply to the data set, simulating the presence of the water above the electrodes.

The Taylor's expansion assumes that the correction for the water layer is relatively small. If this was true for the case illustrated by Hayley et al. (2010), we are here facing a case with significant variations of boundary conditions from no flow to highly conductive. The larger the water layer, the larger the risk to deviate from Taylor's approximation. To validate the approach, we will thus compare the calculated correction to the true correction for a synthetic case where both can be computed.

The approach also assumes that the noise levels are similar. Since $\mathbf{d}_{land,hw}$ is never collected, this is impossible to verify. In practice, the error e between observed and calculated data will be propagated to the corrected data. However, it should be noted that this error is an absolute error expressed in Ohm. As seawater is conductive, the addition of a water layer will globally decrease the resistance. Therefore, if the absolute error is constant, the relative errors will increase proportionally to the decrease of resistance. Those aspects are further discussed in section 3.1.

2.2. Inversion

In this study, we use the 2.5D finite-element forward and inversion code CRTomo (Kemna, 2000). During the inversion, this code minimizes the objective function (Caterina et al., 2014)

$$\psi(\mathbf{m}) = \|W_d(\mathbf{d} - \mathbf{G}(\mathbf{m}))\|^2 + \lambda(\|W_m(\mathbf{m} - \mathbf{m}_{ref})\|^2 + \alpha\|\mathbf{m} - \mathbf{m}_{ref}\|^2), \quad (9)$$

where W_d is the data weighting matrix, \mathbf{d} is the data expressed as the logarithm of the resistance, \mathbf{m} is the model parameter expressed as the logarithm of the electrical resistivity and W_m is the roughness matrix estimating the gradient in the model (de Groot-Hedlin & Constable, 1990), \mathbf{m}_{ref} is the reference model incorporating prior knowledge on the resistivity distribution. The two inversion parameters λ and α are the regularization and closeness factor, respectively. The regularization factor is optimized at each iteration through a line search to minimize the error weighted root-mean-square error (ϵ_{RMS}). The inversion stops when ϵ_{RMS} reaches 1 or when there is no improvement in its value. The closeness factor is fixed during inversion. It is expressed as a diagonal matrix weighting differently each cell of the model according to the user choice (e.g., Dumont et al., 2016).

In our inversion, the closeness factor is used to constrain the conductivity of the water layer to its known value. However, we avoid to use a too large weighting as this can lead to the creation of artifacts (Day-Lewis et al., 2006). Since the presence of a water layer artificially reduces the resolution of land ERT, we also integrate the results of the land ERT inversion at low water level in the reference model. Therefore, for the combined inversion, we have

$$\mathbf{m}_{ref} = \mathbf{m}_{est} + \Delta\mathbf{m}, \quad (10)$$

which corresponds to the model used to estimate $\mathbf{d}_{land,hw}$. For the joint inversion where $\mathbf{d} = [\mathbf{d}_{land,hw} \mathbf{d}_{sea,hw}]$, the corrected land ERT data are already fitted at the beginning of the iterative process. However, adding them in the inversion ensures that any model update will still fit them. The forward and inversion grids used for both data sets are similar, except for the additional presence of the seawater layer.

3. Results

3.1. Synthetic Example

The synthetic model depicting conditions at low (Figure 1a) and high tide (Figure 1c) is inspired by the observed freshwater/saltwater interface in the Western part of the Belgian coast (Vandenbohede & Lebbe, 2006), which is also the location of our field test (see section 3.2). On the beach, a saltwater lens is lying above freshwater, which discharges around the low water line. The peculiar presence of the saltwater lens is due to the dynamical equilibrium of tides on a low sloping shore (Vandenbohede & Lebbe, 2006). The freshwater discharge zone is partly below the low water line and can only be imaged using marine ERT or underwater electrodes. At the elevation of -22 m, a clay layer constitutes the bottom layer of the coastal aquifer (Figure 1a).

Land ERT data are simulated using a multiple gradient array ($s = 8$, $a = 1$ to 6) with 107 electrodes spaced every 5 m from 0 to 530 m (3,456 data points). The last electrode corresponds to the low water line. Marine ERT data are collected using continuous profiling with a reciprocal Wenner-Schlumberger array and 13 electrodes (10 potentials measured simultaneously for each current injection). The electrode spacing is 15 m, and measurements are repeated every 5 m from 175 to 835 m, with a total of 133 electrodes (970 data points). Gaussian white noise (3%) is added on both data sets. All inversion were carried out with the water layer included in a reference model ($\rho = 0.2$ Ohm.m), with $\alpha = 1$ for the corresponding seawater cells, and with a noise level of 3%. We consider marine data collected up to a water layer as thin as 1 m. The 5 m tidal range ensures a wide overlapping of about 350 m between the two data sets.

The inversion of $\mathbf{d}_{land, lw}$ (Figure 1b) clearly indicates the presence of the saltwater lens overlying freshwater. Despite the loss of resolution with depth, it also identifies the underlying clay layer but misses the extension of the discharge zone seaward. When inverted alone (Figure 1d), the marine ERT data $\mathbf{d}_{sea, hw}$ detects the presence of freshwater. Because of the low resolution, it is not clear if the freshwater detected at 500 m extends further seaward compared to the land profile. The higher resistivity on the left side of the profile results from the absence of data in the dune area. The inversion then converges towards the starting model.

If \mathbf{m}_{ref} obtained by inversion of $\mathbf{d}_{land, lw}$ (Figure 1b) is included in the inversion with $\alpha = 0.05$ for the cells below the land profile (Figure 1e), the marine ERT also identifies the freshwater discharge zone. Since the extension seaward is not included in \mathbf{m}_{ref} , we can be more confident that this feature is contained in the data. The saltwater lens is better delineated compared to 1D, although it is less clearly defined than in the land ERT profile. This is because this inversion does not ensure that land ERT data are fitted. Increasing α to 1 solves this issue (Figure 1f), although the extension of the discharge zone seems somehow composed of two distinct zones.

If we correct land ERT data for the high seawater level and invert them jointly with marine data ($\mathbf{d} = -[\mathbf{d}_{land, hw}, \mathbf{d}_{sea, hw}]$, Figure 1g), maintaining $\alpha = 1$, the width of the discharge zone is clearly identified. However, it does not fully extend to the sea bottom. This inversion was ran with a noise level of 3% but converges to $\epsilon_{RMS} = 1.8$. This is related to the increase of the relative error for land ERT data, not taken into account in the prescribed noise level. If the noise level of land ERT is increased to 5% to accommodate the average increase in relative error (Figures 2e and 2f), the inversion converges to a $\epsilon_{RMS} = 1.15$ with almost no modification of the inverted model. A slight additional increase in the noise level would allow to reach $\epsilon_{RMS} = 1$.

In contrast to Hayley et al. (2010), where temperature corrections could be considered small regarding the resistance, the presence of the water layer can significantly modify the resistance data (Figure 2). If the absolute correction is small (Figure 2a), this is because most resistances are very low in highly conductive settings. Therefore, the relative corrections expressed as percentage are large (Figure 2b). The estimated correction is compared to the real difference between $\mathbf{d}_{land, lw}$ and $\mathbf{d}_{land, hw}$ calculated on the synthetic model of Figure 1. We see the proposed methodology properly estimates $\mathbf{d}_{land, hw}$ with only limited deviation (Figure 2c). This is further confirmed on a relative scale: The relative correction is misestimated only for a few points out of the 3,456 resistances of the data set. This is not evidence that the proposed correction can be applied to any case, but it shows that data correction approach can also be applied to a relatively large range of variations in the resistivity model.

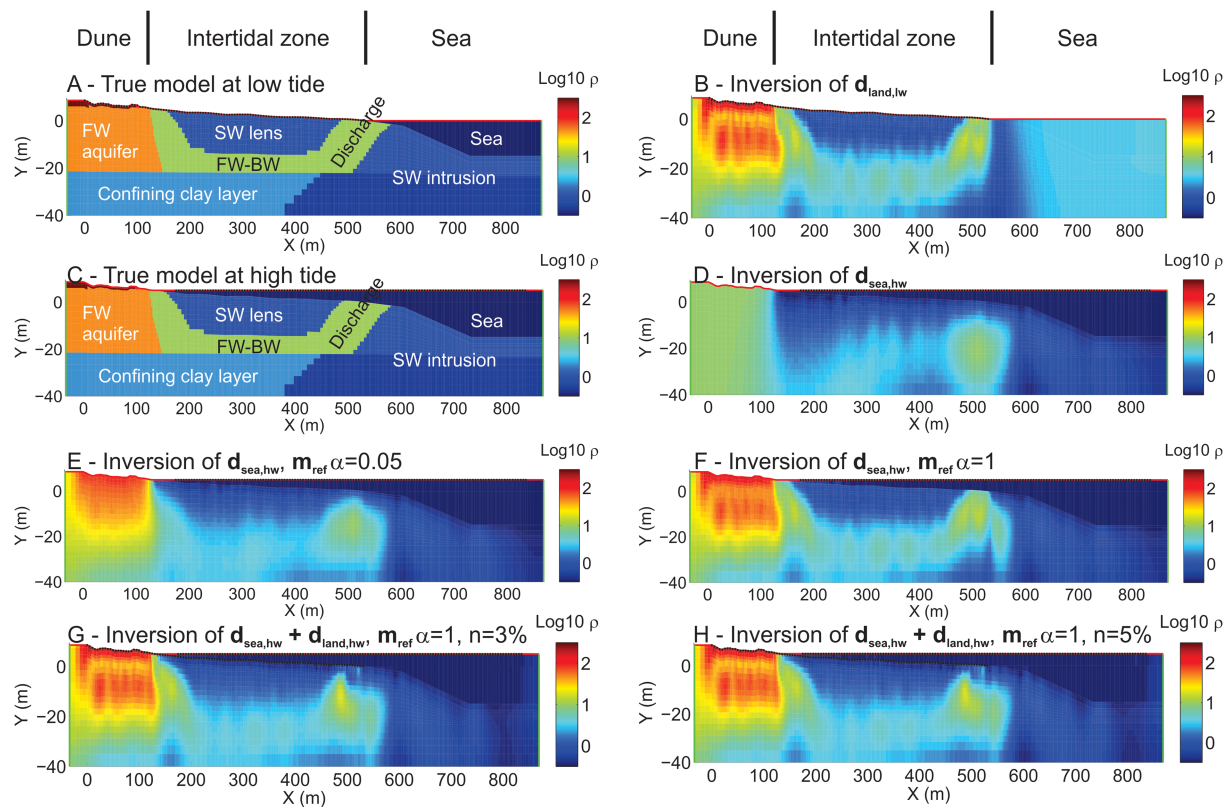


Figure 1. (a) Electrical resistivity distribution at low water level, (b) inversion of $d_{land,lw}$, (c) electrical resistivity distribution at high water level, (d) inversion of $d_{sea,hw}$, (e) inversion of $d_{sea,hw}$ with $m_{ref} \alpha = 0.05$, (f) inversion of $d_{sea,hw}$ with $m_{ref} \alpha = 1$, (g) inversion of $\mathbf{d} = [d_{land,hw} \ d_{sea,hw}]$ with $m_{ref} \alpha = 1$ and noise level for $d_{land,hw}$ at 3%, (h) inversion of $\mathbf{d} = [d_{land,hw} \ d_{sea,hw}]$ with $m_{ref} \alpha = 1$ and increased noise level for $d_{land,hw}$ at 5%. FW, freshwater; SW, saltwater; BW, brackish water.

When we analyze the error level in the data, the average relative error in absolute value in the land ERT data set is 2.33%. Due to the overall decrease of the resistance, related to the negative correction with the presence of the water column, this relative error level increases to 3.94% for the corrected data set. It is thus logical that the inversion with an estimated noise level of 3% cannot converge to an $\epsilon_{RMS} = 1$ as this would mean overfitting the land ERT data.

3.2. Field Case

The field case is located in the Western Belgian coastal plain next to the French border (Figure 3). This site has been largely studied in the past for its characteristic distribution of freshwater and saltwater (Lebbe, 1999; Vandenbohede & Lebbe, 2006). The large recharge in the dune area located to the South, combined with the low slope (1.1%) of the beach and the large tidal range (about 5 m) is responsible for the presence of a saltwater lens above freshwater in the intertidal zone. Recent exploration showed that freshwater discharges in a broad zone ranging from above the low water line to several hundred meters offshore. Characterizing it thus requires the combination of both land and marine ERT profile. Here, we present one of such profiles (Hermans & Paepen, 2019), about 800 m long, with 102 electrodes spaced every 5 m, for a total of 505 m on land (limit of the low water line). Land data were collected using a multiple-gradient array at low tide (-0.15 m). The acquisition protocol was sorted to first use the electrode at the low water line so that electrodes are never under water for measurement despite the rising tide. There is a 230 m overlap with the marine profile (which starts at 270 m on the profile), collected at high tide (3.41 mTAW), which extends 300 m further offshore. The marine data were collected through continuous resistivity profiling, using 13-electrode cables with 15 m spacing and a reciprocal Wenner-Schlumberger array. Data were collected on average every 3.2 m (Figures 3 and 4), together with the height of the water column (bathymetry). Given the rapidity of rising tide for land data and the continuous nature of measurement of marine data, an

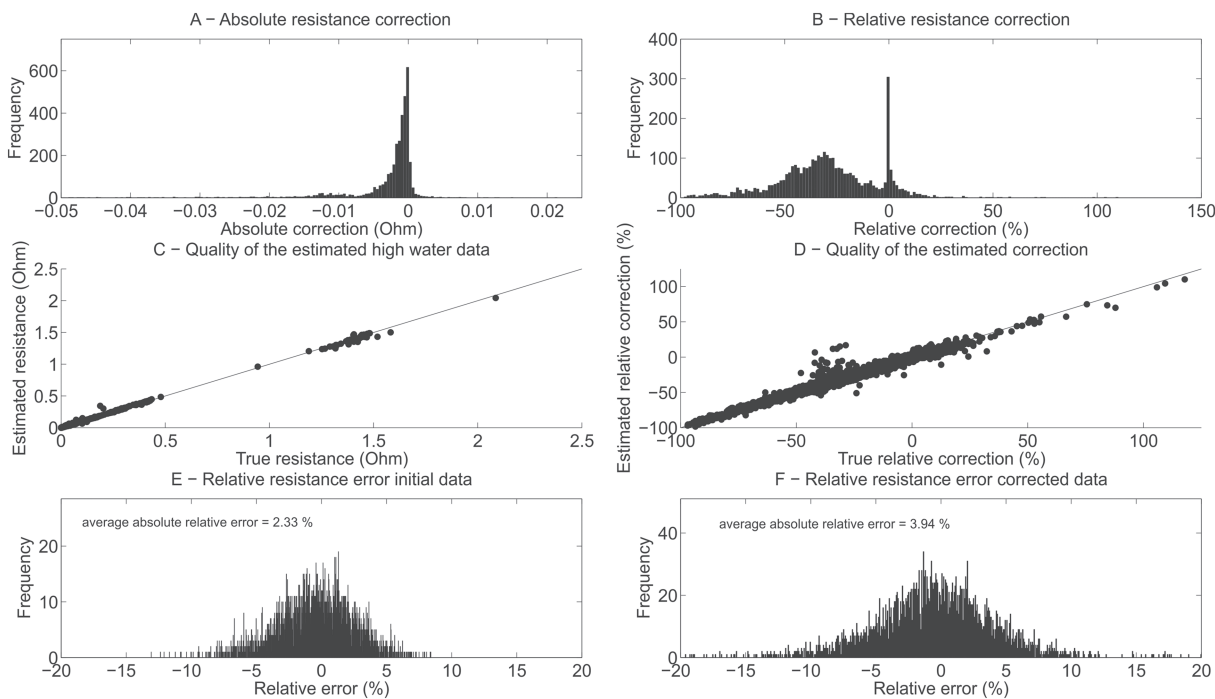


Figure 2. (a) Absolute resistance correction, (b) relative resistance correction, (c) scatterplot of the true and estimated resistance at high water level $\mathbf{d}_{land,hw}$, (d) scatterplot of the true and estimated relative correction at high water level, (e) relative error in the original data set, (f) relative error in the corrected data set.

estimation of the error through reciprocals is not available. It was estimated at about 3% for both data sets. Applying the methodology to field data assumes that the resistivity distribution is not strongly varying between low and high tide conditions. Vandenbohede and Lebbe (2007) showed that the tide dynamic is not significantly affecting the salt water distribution in the area. Only local changes at the sea interface are expected due to the infiltration of seawater during high tide. Those are low compared to the influence of the seawater layer. The global distribution of resistivity is mostly affected by seasonal variations.

The inversion results confirm the observations made with the synthetic case (Figure 4). The inversion of $\mathbf{d}_{land,tw}$ allows to clearly image the saltwater lens ($\rho < 3 \text{ Ohm.m}$, $\log \rho < 0.5$) as well as the discharge zone ($\rho > 10 \text{ Ohm.m}$, $\log \rho > 1$) close to the low water line between 380 and 480 m along the profile (Figure 4a). It is however not clear if fresh to brackish water is present seawards. At the beginning of the profile, the freshwater aquifer in the dune is identified with high resistivity ($\rho > 100 \text{ Ohm.m}$, $\log \rho > 2$). The homogeneous resistivity on the right side of the profile is due to the absence of data, the solution converges towards the starting model. In the inversion of $\mathbf{d}_{sea,hw}$, the freshwater is detected under the intertidal zone, but not as precisely as with $\mathbf{d}_{land,tw}$ (Figure 4b). Nevertheless, the marine data reveal the presence of fresher water to at least 700 m along the profile, that is, 200 m away from the low water line. Adding \mathbf{m}_{ref} ($\alpha = 1$) from land data inversion (Figure 4b) enables to combine the two solutions, what confirms the presence of freshwater below the low water line (Figure 4c).

As for the synthetic case, the presence of \mathbf{m}_{ref} with $\alpha = 1$ ensures that the land inverted model is recovered after inversion of the sea data. However, it does not ensure that the land data are still explained to their noise level. Therefore, we apply the proposed methodology to the field data, and the corrected land data $\mathbf{d}_{land,hw}$ is computed and inverted together with the sea data $\mathbf{d} = [\mathbf{d}_{land,hw} \mathbf{d}_{sea,hw}]$. To accommodate the artificial increase of the relative noise level (Figure 2), we adopt a noise level for $\mathbf{d}_{land,hw}$ of 5%.

This data set is first inverted without \mathbf{m}_{ref} (except for the presence of seawater layer). The first 200 m of the model are quite similar to the land inverted model, because the correction is minimal (Figure 4d). In the overlapping zone, however, the resolution of land ERT data is artificially decreased by the presence of the water layer, and the inversion result is somewhere between Figures 4a and 4b. The discharge zone is better imaged than with marine data only, but not as accurately as with land data only. This is confirmed by the

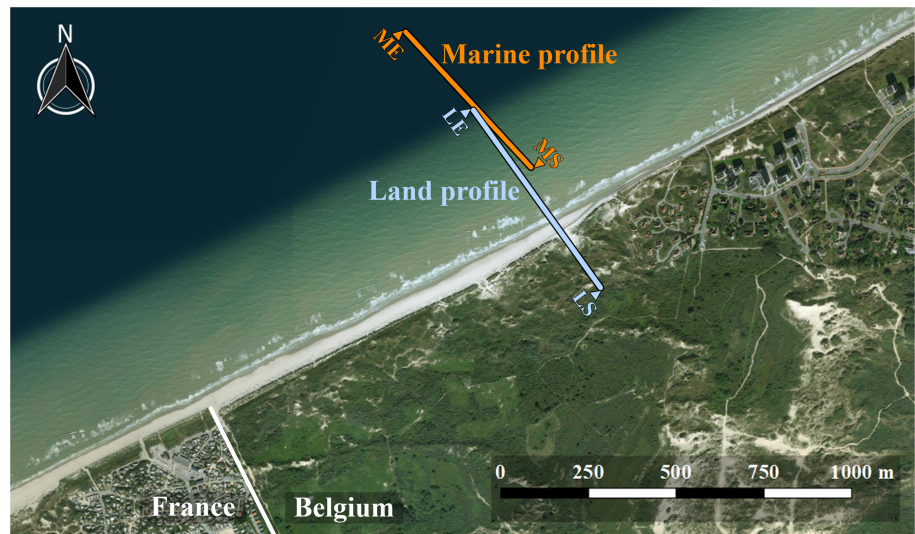


Figure 3. Field site and localization of land and marine profiles. LS and LE indicate the start and end of the land profile, MS and ME the start and end of the marine profile.

normalized cumulative sensitivity distribution (Figure 4f), where a lateral decrease of sensitivity is observed due to the presence of seawater. Whereas for land data alone no strong lateral variations are expected, except at the extreme edge of the profile. The identification of freshwater on the seaside is reinforced. Adding a

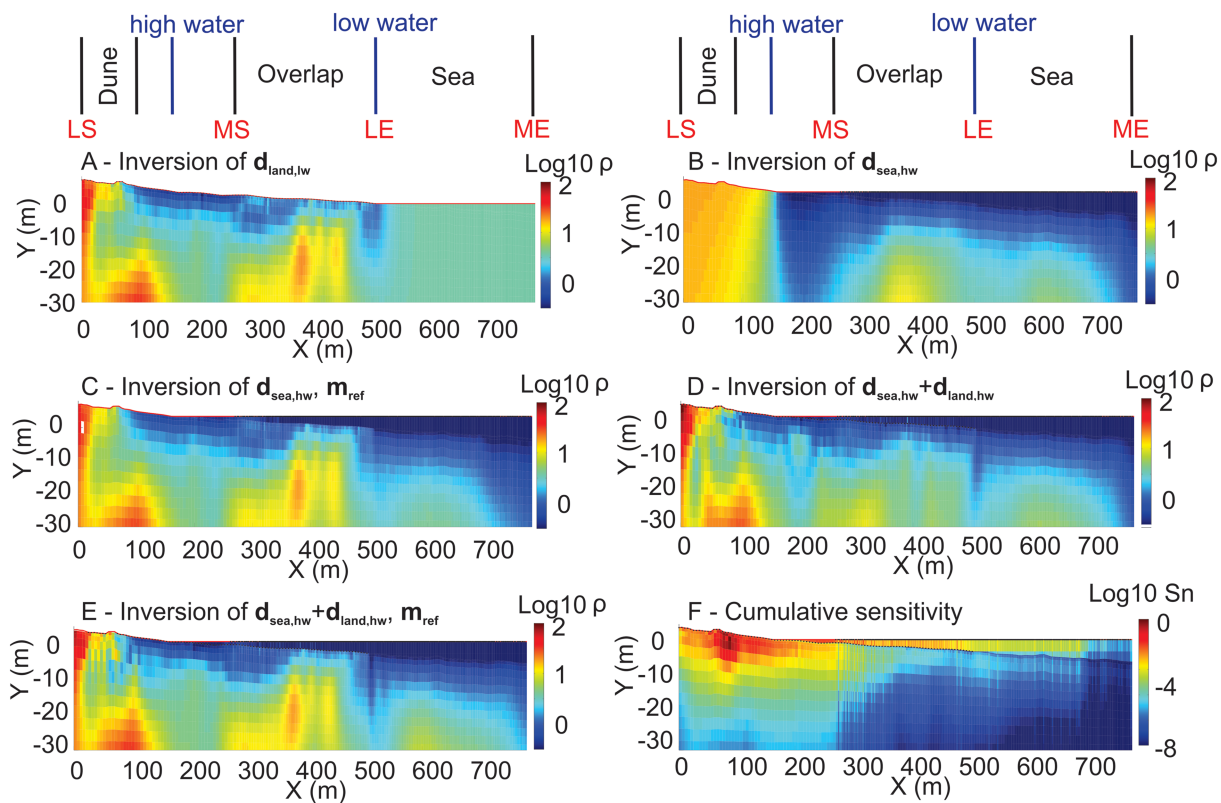


Figure 4. Field data inversion. (a) Inversion of $d_{land,hw}$, (b) inversion of $d_{sea,hw}$, (c) inversion of $d_{sea,hw}$ with $m_{ref} (\alpha = 1)$, (d) inversion of $\mathbf{d} = [d_{land,hw} \ d_{sea,hw}]$ without m_{ref} , (e) inversion of $\mathbf{d} = [d_{land,hw} \ d_{sea,hw}]$ with $m_{ref} (\alpha = 1)$, (f) normalized cumulative sensitivity distribution corresponding to the results of Figure 4d. LS and LE indicate the start and end of the land profile, MS and ME the start and end of the marine profile.

reference model with $\alpha = 1$ (Figure 4e) corrects this effect by limiting the deviation to the land model in the overlapping zone and likely provides the best model, ensuring that the high resolution data of the land profile are optimally integrated in the inversion, while also fitting sea data.

Few differences between Figures 4c and 4e are observed in this specific case, except around the last land electrode, as observed for the synthetic test. This zone is thus more sensitive to the proposed methodology. Nevertheless, the combined inversion (Figure 4e) yields results with slightly larger resistivity values below the sea, confirming the freshwater flux. In this case, the low sensitivity of the sea data is not sufficient to overcome the large weight given to the reference model under the land part of the profile. This observation might not hold for any case study as it strongly depends on the thickness of the water layer, its conductivity, and on the choice of the notation defined in section 2.2. As stated previously, the combined solution ensures that the data misfit from the land data is still considered in the joint inversion, avoiding undesired changes. The low resolution of marine data prevents us to make definitive conclusion about the depth and actual resistivity of the freshwater on the sea side. Indeed, the low resistivity spotted below the seawater layer is largely influenced by this conductive body, reducing the imaging capability of the method.

4. Conclusion

In this contribution, we propose a new methodology to jointly invert land and marine ERT data collected along the same profile. We first invert the land ERT data alone to have a first estimate of the electrical resistivity distribution in the subsurface. This estimated model is used to calculate a correction factor to apply to the land ERT data to be able to invert them jointly with the marine ERT in high water level conditions. We demonstrate that the data correction approach is accurate and sufficiently efficient even if the seawater layer induces large changes in resistivity and current flow patterns. However, to counterbalance the artificial loss of resolution of land ERT data due to the presence of seawater, the estimated model is also used as a reference model during inversion. Similarly, the correction factor implies an artificial increase in the estimated noise level that has to be accounted for.

Land ERT alone does not generally extend far enough to identify SGD, whereas the resolution of marine ERT is often not sufficient to identify accurately where freshwater actually discharges. The combined inversion of land and marine ERT helps to better define the freshwater/saltwater distribution in coastal aquifers, mostly because the knowledge of the resistivity distribution from the land profile allows to constrain information collected with marine ERT. Significant improvement is observed on the seaside limit of the land profile.

Our methodology has been demonstrated for the characterization of the freshwater/saltwater interface in the intertidal zone and beyond. In this case, the use of a strong reference model might be sufficient to optimize the final image. However, this solution does not ensure that the final model fits both land and marine ERT. This behavior might not be observed in other cases. Our approach assumes that the global distribution of resistivity (or salinity) is not significantly affected by the tide cycle. This is the case for our case study where the salinity distribution is in dynamical equilibrium. This is not necessarily the case for all shorelines and all measurement scales. By extension, our approach could also be applied for monitoring with partially submerged electrodes (depending on the tides). In such a case, the application of time-lapse inversion scheme would also require to correct the data for the water column. The same approach can also be used to invert ERT profiles acquired at any different tide levels.

Acknowledgments

This research was funded by the Flemish Science Foundation (FWO) grant numbers 1505219N and SN003719N and the Flemish Institute for the Sea (VLIZ) Brilliant Marine Research Idea 2018. We thank Liège University for lending us the land ERT equipment. The field data set (Hermans & Paepen, 2019) is published and openly available on the VLIZ database <http://www.vliz.be/en/imis?module=dataset&dsid=6373>.

References

- Attwa, M., Günther, T., Grinat, M., & Binot, F. (2011). Evaluation of DC, FDEM, and IP resistivity methods for imaging perched saltwater and a shallow channel within coastal tidal flat sediments. *Journal of Applied Geophysics*, 75, 656–670. <https://doi.org/10.1016/j.jappgeo.2011.09.002>
- Befus, K. M., Cardenas, M. B., Tait, D. R., & Erler, D. V. (2014). Geoelectrical signals of geologic and hydrologic processes in a fringing reef lagoon setting. *Journal of Hydrology*, 517, 508–520. <https://doi.org/10.1016/j.jhydrol.2014.05.070>
- Bratton, J. F. (2010). The three scales of submarine groundwater flow and discharge across passive continental margins. *The Journal of Geology*, 118(5), 565–575. <https://doi.org/10.1086/655114>
- Cardenas, M. B., Zamora, P. B., Siringan, F. P., Lapus, M. R., Rodolfo, R. S., Jacinto, G. S., et al. (2010). Linking regional sources and pathways for submarine groundwater discharge at a reef by electrical resistivity tomography, ^{222}Rn , and salinity measurements. *Geophysical Research Letters*, 37(16), L16401. <https://doi.org/10.1029/2010GL044066>
- Caterina, D., Hermans, T., & Nguyen, F. (2014). Case studies of incorporation of prior information in electrical resistivity tomography: Comparison of different approaches. *Near Surface Geophysics*, 12, 451–465. <https://doi.org/10.3997/1873-0604.2013070>

- Day-Lewis, F. D., White, E. A., Johnson, C. D., Lane, J. W. J., & Belaval, M. (2006). Continuous resistivity profiling to delineate submarine groundwater discharge-examples and limitations. *The Leading Edge*, 6(25), 724–728. <https://doi.org/10.1190/1.2210056>
- de Groot-Hedlin, C., & Constable, S. (1990). Occam's inversion to generate smooth, two-dimensional models from magnetotelluric data.. *Geophysics*, 55(12), 1613–1624. <https://doi.org/10.1190/1.1442813>
- Dumont, G., Pilawski, T., Dzaomuho-Lenieregue, P., Hilgsmann, S., Delvigne, F., Thonart, P., et al. (2016). Gravimetric water distribution assessment from geoelectrical methods (ERT and EMI) in municipal solid waste landfill. *Waste Management*, 55, 129–140. <https://doi.org/10.1016/j.wasman.2016.02.013>
- Goebel, M., Pidlisecky, A., & Knight, R. (2017). Resistivity imaging reveals complex pattern of saltwater intrusion along Monterey coast. *Journal of Hydrology*, 551, 746–755. <https://doi.org/10.1016/j.jhydrol.2017.02.037>
- Hayley, K., Bentley, L. R., & Pidlisecky, A. (2010). Compensating for temperature variations in time-lapse electrical resistivity difference imaging. *Geophysics*, 75(4), WA51–WA59. <https://doi.org/10.1190/1.3478208>
- Henderson, R. D., Day-Lewis, F. D., Abarca, E., Harvey, C. F., Karam, H. N., Liu, L., & Lane, J. W. (2010). Marine electrical resistivity imaging of submarine groundwater discharge: Sensitivity analysis and application in Waquoit Bay, Massachusetts, USA. *Hydrogeology Journal*, 18(1), 173–185. <https://doi.org/10.1007/s10040-009-0498-z>
- Hermans, T., & Paepen, M. (2019). Land and Marine ERT data set collected across the shoreline at the Westhoek nature reserve. *Marine Data Archive, Flanders Marine Institute*. <https://doi.org/10.14284/390>
- Hermans, T., Vandenbohede, A., Lebbe, L., Martin, R., Kemna, A., Beaujean, J., & Nguyen, F. (2012). Imaging artificial salt water infiltration using electrical resistivity tomography constrained by geostatistical data. *Journal of Hydrology*, 438–439, 168–180. <https://doi.org/10.1016/j.jhydrol.2012.03.021>
- Kemna, A. (2000). *Tomographic inversion of complex resistivity-theory and application*. Bochum, Germany: Ruhr-Universität.
- Kwon, E. Y., Kim, G., Primeau, F., Moore, W. S., Cho, H., DeVries, T., et al. (2014). Global estimate of submarine groundwater discharge based on an observationally constrained radium isotope model. *Geophysical Research Letters*, 41(23), 8438–8444. <https://doi.org/10.1002/2014GL061574>
- Lebbe, L. (1999). Parameter identification in fresh-saltwater flow based on borehole resistivities and freshwater head data. *Advances in Water Resources*, 22(8), 791–806. [https://doi.org/10.1016/S0309-1708\(98\)00054-2](https://doi.org/10.1016/S0309-1708(98)00054-2)
- Loke, M. H., Chambers, J. E., Rucker, D. F., Kuras, O., & Wilkinson, P. B. (2013). Recent developments in the direct-current geoelectrical imaging method. *Journal of Applied Geophysics*, 95, 135–156. <https://doi.org/10.1016/j.jappgeo.2013.02.017>
- Nguyen, F., Kemna, A., Antonsson, A., Engesgaard, P., Kuras, O., Ogilvy, R., et al. (2009). Characterization of seawater intrusion using 2D electrical imaging. *Near Surface Geophysics*, 7(5–6), 377–390. <https://doi.org/10.3997/1873-0604.2009025>
- Post, V. E. A., Groen, J., Kooi, H., Person, M., Ge, S., & Edmunds, W. M. (2013). Offshore fresh groundwater reserves as a global phenomenon. *Nature*, 504(7478), 71–78. <https://doi.org/10.1038/nature12858>
- Taniguchi, M., Burnett, W. C., Cable, J. E., & Turner, J. V. (2002). Investigation of submarine groundwater discharge. *Hydrological Processes*, 16(11), 2115–2129. <https://doi.org/10.1002/hyp.1145>
- Taniguchi, M., Ishitobi, T., & Shimada, J. (2006). Dynamics of submarine groundwater discharge and freshwater-seawater interface. *Journal of Geophysical Research*, 111, C01008. <https://doi.org/10.1029/2005JC002924>
- Vandenbohede, A., & Lebbe, L. (2006). Occurrence of salt water above fresh water in dynamic equilibrium in a coastal groundwater flow system near De Panne, Belgium. *Hydrogeology Journal*, 14(4), 462–472. <https://doi.org/10.1007/s10040-005-0446-5>
- Zhou, Y., Sawyer, A. H., David, C. H., & Famiglietti, J. S. (2019). Fresh Submarine Groundwater Discharge to the Near-Global Coast. *Geophysical Research Letters*, 2019GL082749, 46(11), 5855–5863. <https://doi.org/10.1029/2019GL082749>